PHYSICAL REVIEW B VOLUME 48, NUMBER 23 15 DECEMBER 1993-I

Interfacial roughness of sputtered multilayers: Nb/Si

Eric E. Fullerton, J. Pearson, C. H. Sowers, and S. D. Bader
Materials Science Division, Argonne National Laboratory, Argonne, Illinois 60439

X. Z. Wu and S. K. Sinha
Exxon Research and Engineering Company, Annandale, New Jersey 08801
(Received 19 April 1993; revised manuscript received 27 September 1993)

We have carried out studies of the interfacial roughness of a number of Nb/*a*-Si multilayers using cross-section transmission electron microscopy, wide-angle x-ray diffraction, and low-angle x-ray reflectivity and diffuse scattering. The multilayers studied were grown by sputtering in an Ar atmosphere at various pressures. The effect of the layer thickness and of the number of layers has also been studied. We observed a clear transition in the growth morphology when the sputtering pressure is raised above the thermalization pressure (≈ 9 mTorr) of the sputtered atoms. Both the mosaic of the Nb crystallites and the interface roughness increase dramatically when the Ar pressure exceeds 9 mTorr. The roughness of the various interfaces is strongly conformal and the samples with large roughness show a roughness that increases with deposited layer number. We discuss the quantitative extraction of these parameters from the x-ray data and the implications of these results for the physics of the deposition process.

I. INTRODUCTION

There are interests in multilayer structures for both scientific and practical applications.[1] This is because adjustment of the thicknesses of the constituent layers makes it possible to probe physical phenomena of thin films and interfaces, and the coupling of adjacent layers. However, a major limitation in understanding the physics stems from the nonequilibrium deposition techniques used to synthesize multilayers. The structure obtained is very sensitive to a number of deposition parameters. To quantitatively understand the physical properties requires the determination of the type and characteristic length scale of structural disorder present in the multilayer.

Considerable experimental and theoretical efforts have been focused on understanding the kinetic and thermodynamic factors that control the growth of both thin films and multilayers.[2,3] For thin films a number of theoretical models predict that the width of the growth interface (σ) scales with film thickness (t) by the general relation $\sigma \approx t^{\beta}$.[4–7] The dynamic scaling exponent β depends on the dimensions of the surface and the specific assumptions of the model. Recent experimental studies have determined a range of values ($\beta \approx 0.2-0.5$) depending on deposition conditions.[8–11] For sputtered films in which the substrate temperature is low compared to the melting temperature of the deposited material (known as "zone 1" growth), the expected surface morphology consists of domed columns. The columns have a characteristic lateral length scale ξ which scales with thickness as $\xi \approx t^{p}$. The scaling exponent p also has been studied both theoretically[12–14] and experimentally.[15,16]

For a multilayer structure, it may be expected that the roughness would scale with the total film thickness in a similar fashion to thin films. The implication of this is that the roughness per interface (both σ and ξ) will increase with an increasing number of bilayers. Such behavior has been observed in some multilayers.[17,18] In other cases, it has been found that the interface roughness depends more strongly on the constituent layer thicknesses than on the total film thickness.[19] For instance, a deposited layer can "heal" the roughness of the previous layer (or of the substrate),[20] depending on thermodynamic quantities such as the surface free energy and the heat of mixing. The formation of interfacial compounds also can alter the stability of the multilayer structure. In general, the propagation of roughness within multilayers depends on the lateral frequency of the roughness, the thermodynamic properties of the constituent layers, and on the kinetic properties of the deposited atoms in a way that is not completely understood.

Multilayer roughness can be divided into different generic types that involve correlated and uncorrelated behavior as additional bilayers are added to the stack. The roughness of an individual layer can be characterized by length scales, such as σ and ξ introduced above, or by frequency components of the interfacial corrugation.[21] Self-similar behavior can be characterized by a fractal dimension. Then the layer-to-layer correlation needs to be considered. Perfectly correlated behavior is known as "conformal" roughness. Increased roughness from one layer to the next is known as "cumulative" roughness. An opposite extreme to these cases would involve totally uncorrelated roughness from one layer to the next where the fluctuations of a given interface are independent of the previous interfaces. In most cases, the situation may best be described as lying between these extremes. Figure 1 shows a schematic of these generic roughness types.

In this paper we utilize x-ray diffraction (XRD) and cross-section transmission electron microscopy (XTEM)

 ©1993 The American Physical Society

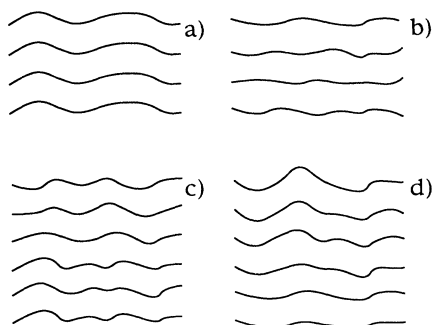

FIG. 1. Schematic representation of interface roughness in multilayers: (a) perfectly conformal roughness, (b) uncorrelated interface roughness, (c) partially correlated roughness in which the total roughness per interface is constant, and (d) partially correlated roughness which is cumulative.

to study the influence of Ar sputtering pressure on the growth of Nb/Si multilayers. Nb/Si provides an instructive case because extremely smooth, as well as conformal and cumulative roughness cases can be realized by adjustment of the sputter conditions. Nb/Si is desirable because its elemental scattering factors provide suitable contrast for successful XRD and XTEM studies. Additionally, there is continued interest in metal/Si multilayers as x-ray optical elements. The growth dynamics is strongly affected by the kinetic properties of the deposited atoms which vary greatly with Ar pressure.[22] At low Ar pressure, the atoms impinge on the substrate with several electron volts of energy and nearly ballistic trajectories. At high Ar pressure, the impinging atoms are thermalized by the sputtering gas and have nearly random trajectories. We have varied the Ar pressure from 3 to 15 mTorr. This spans the range from high kinetic energy to thermalized deposited atoms where the expected pressure for thermalization is ~ 9 mTorr for our target-substrate distance.[22]

We find that there is a clear transition in the growth morphology at the thermalization pressure. For multilayers sputtered at low pressures (<9 mTorr) smooth, flat layers form with (110)-textured Nb grains and the interface roughness is nearly independent of film thickness. At high pressure, domed columns of polycrystalline Nb grains develop and grow as the film thickens. In addition to studying the systematics as a function of Ar pressure for a set of films with fixed Nb layer, Si layer, and total thickness, we also studied a subset of films with a different number of bilayers, to vary the total films thickness, and with the same total thickness but twice the nominal component layer thickness. These studies taken together provide a rather representative overview of sputter-growth conditions.

The remainder of the paper is organized as follows. Section II provides basic experimental details. Sections III and IV introduce the XTEM and low- and wide-angle XRD results, respectively. The real space images of Sec. III permit reasonable assumptions to be formulated in order to obtain a quantitative understanding of the XRD data. Section V is devoted to modeling the low-angle XRD data. Two types of models are considered. For the first model the interfacial width is assumed constant and layer-thickness errors are analyzed. For the second model the layer thicknesses are fixed and the interfacial widths are varied. Section VI provides a general discussion of kinetic and thermodynamic factors that influence multilayer growth. Finally, Sec. VII is devoted to a brief overview of our major findings.

II. EXPERIMENTAL PROCEDURE

The Nb/Si multilayers we grown by dc magnetron sputtering with a target-substrate distance of 9 cm. A Microscience system was used that is turbopumped to a system base pressure of 10^{-8} Torr, as in previous studies.[23] Samples studied included $[\mathrm{Nb}(\approx 35\ \text{Å})/\mathrm{Si}(\approx 30\ \text{Å})]_N$ (where $N=10$ and 40) and $[\mathrm{Nb}(\approx 70\ \text{Å})/\mathrm{Si}(\approx 60\ \text{Å})]_{20}$ sputtered at pressures ranging from 3 to 15 mTorr. This choice of samples permitted cumulative as well as individual layer thickness effects to be monitored. All films were grown onto sapphire substrates at ambient temperature. The sputtering rates were set by crystal monitors and were kept constant for all sputtering pressures. To achieve constant rates requires adjusting the sputtering parameters (i.e., current and voltage.) The voltage (current) parameters for the Nb and Si targets range from 350 V (0.63 A) and 450 V (0.32 A), respectively, at 3 mTorr to 320 V (0.82 A) and 530 V (0.56 A) at 15 mTorr. The increased sputtering power at higher sputtering pressures is required to compensate for the loss of flux which occurs from scattering with neutral Ar atoms. The layer thicknesses were determined by the rotation rate of the substrate over the Nb and Si targets. As a further check on the thickness calibration of the films an additional set of films was made at 3 and 11 mTorr with the Si sputtering gun turned off to determine the Nb thicknesses. The layer thicknesses determined from the low-angle XRD finite-size peaks of the film were 36 and 34 Å for the 3- and 11-mTorr samples.

Wide-angle XRD was carried out on a Rigaku powder diffractometer using Cu $K\alpha$ radiation. Low-angle XRD data were obtained at the National Synchrotron Light Source at Brookhaven National Laboratory on beamline X-22C using $\lambda=1.53$ Å radiation determined by a Ge double crystal. The beam size is defined by the slits settings in front of the sample, that is, 0.3 mm vertically and 2 mm horizontally. The detector slit is set accordingly as 0.5 mm vertically and 3 mm horizontally to include all the main beam and specular reflection intensity. The ultimate resolution is $\Delta\theta \approx 0.026°$ or $\Delta q_z \approx 3.7\times 10^{-3}$ Å^{-1}. The samples are macroscopically flat resulting in the reflected beam having the same width as the main one. The footprint correction has been made to consider only the part of the beam projected on the sample at small angles. XTEM images were obtained on a JEOL 100 CX STEM operating at 100 kV at the Electron Microscopy Center at Argonne National Laboratory. The XTEM samples were prepared by conventional cross-sectioning techniques. Ion milling of the dimpled samples with 5-kV Ar ions while the sample is maintained at a temperature of 77 K produced electron transparent areas. Digitized XTEM images were psuedocolorized using IMAGE

public-domain software run on a Macintosh IIfx computer. XRD modeling was performed on a VAXstation 3100 using a modification of the FORTRAN code developed by Fullerton *et al.*[24]

III. TRANSMISSION-ELECTRON-MICROSCOPY RESULTS

Shown in Figs. 2(a) and 2(b) are the XTEM images of the $[Nb(\approx 35\ Å)/Si(\approx 30\ Å)]_{40}$ multilayers sputtered at 3 and 15 mTorr, respectively. The difference between the two images is quite striking. The XTEM image of the 3-mTorr sample shows smooth and continuous layers over the entire cross section with no obvious changes in morphology from one layer to the next, while the image of the 15-mTorr sample shows that both the interfacial roughness and morphology change with subsequent layers. For the 15-mTorr sample the initial layers are smooth, but, as the growth progresses, fluctuations develop in the layer thickness and result in the growth of domed columns with well-defined grains boundaries. Such behavior is characteristic of zone-1 thin-film growth. XTEM images of the 9-mTorr sample were similar to those of the 3-mTorr sample in that they lack the formation of domed columns and grain boundaries. A similar dependence on Ar pressure has been observed for other metal/Si (Refs. 25 and 26) and metal/metal multilayers.[18,27]

(a)

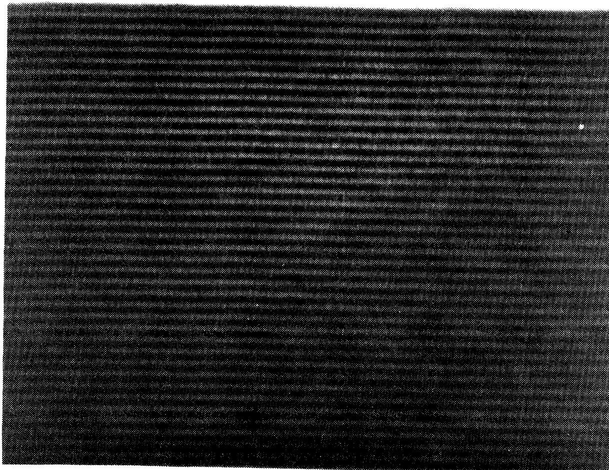

(b)

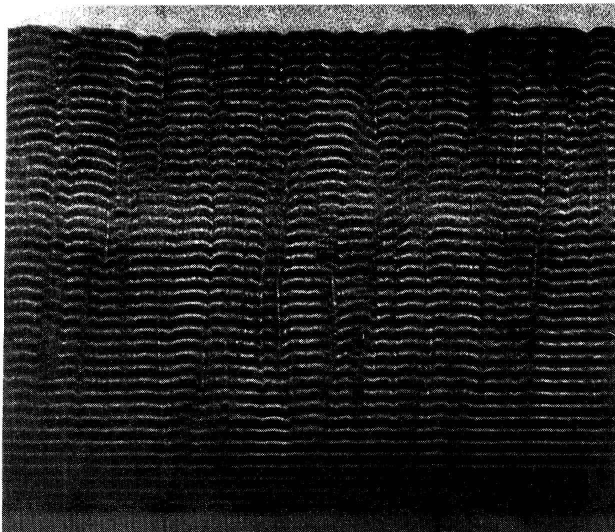

FIG. 2. XTEM images of $[Nb(35\ Å)/Si(30\ Å)]_{40}$ multilayers sputtered in (a) 3 mTorr and (b) 15 mTorr of Ar.

The digitized images of Figs. 3(a) and 3(b) show expanded views of Figs. 2(a) and 2(b). Figure 3(a) is characteristic of a number of metal/amorphous-semiconductor multilayers.[25,26,28–32] While there is some interfacial roughness, the layers appear smooth, in general, with no obvious increase in roughness from layer to layer. Figure 2(b) shows highly conformal, curved growth fronts separated by grain boundaries. The average grain size in Fig. 2(b) is of the order 100–200 Å.

Although the morphology of the interfaces is quite different in Figs. 3(a) and 3(b), the sharpness of the interfaces is similar. Shown in Fig. 4 is the intensity contrast measured normal to layers for the images shown in Figs. 3(a) and 3(b). Care must be taken in the interpretation of XTEM images because they result from projections of the interface over the specimen thickness. Factors such as multiple scattering, misalignment of the sample relative to the electron beam, and the electron optical defocus parameters can also influence the images.[33] However, within the resolution of our images, there is no qualitative difference in the interfacial width between the 3- and 15-mTorr samples. There is, however, a systematic difference between the Nb-on-Si and the Si-on-Nb interfaces observed in Fig. 4. The Si-on-Nb interface is sharper than the Nb-on-Si interface. This observation is consistent with a number of other studies of metal/Si multilayers.[25,26,28–32,34–36]

IV. X-RAY-DIFFRACTION RESULTS

A. Wide-angle XRD data

Selected wide-angle diffraction data are shown in Fig. 5(a) and are similar to other crystalline-amorphous multilayers.[37] A single broad peak near the expected Nb(110) position is observed. The continuous fluctuations intrinsic to the amorphous-Si layer result in the Nb layers scattering incoherently from each other. The diffraction scan is characteristic of a single-crystalline layer. Shown in Fig. 5(b) is the mosaic spread of the crystallites obtained from the widths of rocking-curve scans through the Nb(110) peak. For the low-pressure samples, the finite-size oscillations indicate that there is a well-defined crystal thickness value and a high degree of crystallographic orientation. As the pressure increases, the intensity decreases, the mosaic spread increases, and the finite-size oscillations are damped out.

The θ-2θ peak width and/or the separation of the finite-size oscillations are a measure of the crystal coherence length within the layer. The crystal coherence length is found to be nearly independent of the Ar pressure. For the 35- and 70-Å Nb layers, the crystal coherence is ≈ 26 and ≈ 56 Å, respectively. For both sets of films the crystal coherence is less than the Nb thickness determined from the low-angle diffraction data.

(a)

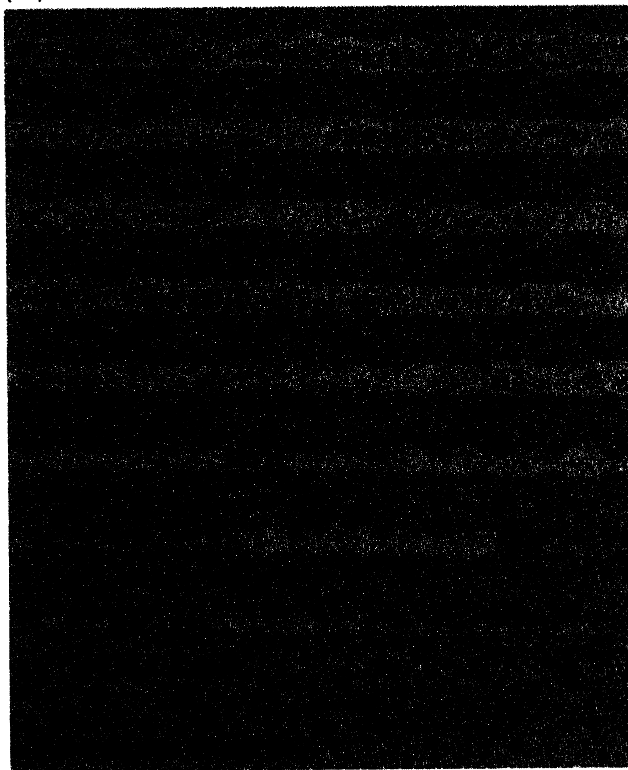

(b)

FIG. 3. Digitized and pseudocolor enhanced XTEM images from Fig. 1 corresponding to multilayers sputtered in (a) 3 mTorr and (b) 15 mTorr of Ar.

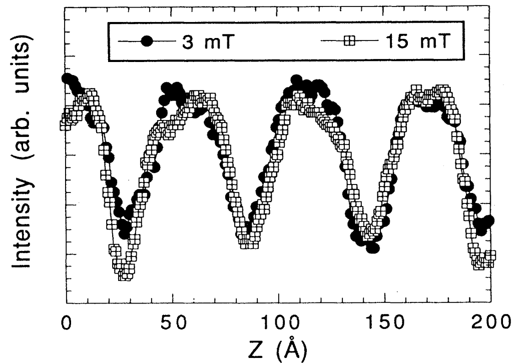

FIG. 4. Intensity-contrast scans normal to the layer obtained from the images in Figs. 3(a) and 3(b).

B. Low-angle XRD data

Low-angle x-ray-diffraction scans were taken to measure both the diffuse and specular scattered intensities.[38] Both longitudinal and transverse scans shown schematically in Fig. 6 were obtained. The longitudinal scans provide information about correlation of the interface roughness of different interfaces, while the transverse scans are sensitive to the height-height correlation function and lateral coherence length of the interface roughness. Figure 7 shows the specular and diffuse components of a 5-mTorr [Nb(35 Å)/Si (30 Å)]$_{10}$ multilayer and the multilayers shown in Fig. 2 as a function of q_z. The longitudinal diffuse component was measured just off the specular ridge by offsetting the scattering vector 0.055° relative to the sample normal, as shown in Fig. 6. The specular components shown in Fig. 7 are the total intensity measured at the specular condition minus the diffuse intensity. The specular component for the samples grown at low Ar pressures [Figs. 7(a) and 7(b)] have well-defined Bragg reflections out to high order. In addition to the Bragg peaks, higher-frequency oscillations resulting from the finite thickness of the multilayer are clearly observed in Fig. 7(a). The inset to Fig. 7(b) shows that finite-size oscillations between the fourth and fifth Bragg reflection are still observed for a multilayer with a total thickness of ≈2500 Å. The XRD spectrum of the 15-mTorr sample is qualitatively different, as was found for the XTEM images. There is a limited number of Bragg peaks and the peak widths increase with increased order of the diffraction peaks. This results from the cumulative nature of the disorder.[24,39] For all three samples, the longitudinal diffuse spectra are peaked at the same q_z values as the specular features. This indicates that the interfacial roughness is at least partially correlated from one layer to the next.[19,38–40] Finite-size peaks also are observed in the diffuse scan in Fig. 7(a). This indicates that the interfaces are correlated over the total thickness of the multilayer. This correlation of the interfacial roughness is seen as well in the XTEM images of the 15-mTorr sample. For low Ar pressure, the correlated nature of the rough-

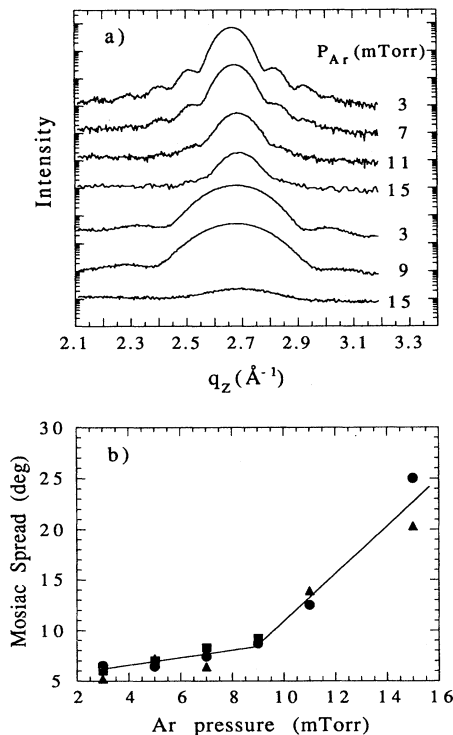

FIG. 5. (a) Wide-angle diffraction scans about the Nb(110) reflection for [Nb(70 Å)/Si(60 Å)]$_{20}$ at 3, 7, 11, and 15 mTorr and [Nb(35 Å)/Si(30 Å)]$_{40}$ multilayers sputtered at 3-, 9-, and 15-mTorr Ar pressures. (b) Wide-angle rocking curve widths $\Delta\theta$ vs Ar pressure for [Nb(35 Å)/Si(30 Å)]$_{10}$ (circles), [Nb(35 Å)/Si(30 Å)]$_{40}$ (squares), and [Nb(70 Å)/Si(60 Å)]$_{40}$ (triangles).

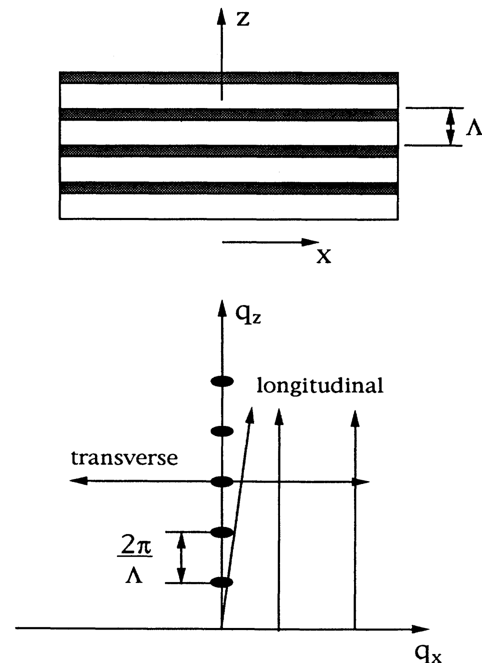

FIG. 6. Schematic representation of multilayer structure in real space and scattering geometry in reciprocal space. Multilayer Bragg reflections are represented by ovals on the q_z axis separated by $2\pi/\Lambda$. Transverse scans are measured parallel to the q_x axis and longitudinal scans are measured either parallel or slightly angled with respect to the q_z axis.

ness is more subtle and beyond the resolution of our XTEM measurements.

Shown in Fig. 8(a) is a transverse scan through the $q_z = 0.4$ Å^{-1} diffraction peak of Fig. 7(a). The scan contains the specular peak at $q_x = 0.0$ Å^{-1} and a broad diffuse component. The width of the diffuse component increases with q_z but is typically of the order of the inverse of the lateral coherence length of the roughness at a measured value of q_z.[19,38,40] The width indicates that the lateral coherence is comparable to that of other crystalline/amorphous multilayers,[19,38,40] but short, for example, in comparison to GaAs/AlAs superlattices.[41,42] The shape of the diffuse component depends on both the lateral coherence length and details of the height-height correlation function needed to characterize the interfacial roughness.[21,43] (The fittings of the diffuse component to a general height-height correlation function are in progress and will be presented elsewhere.[44]) Shown in Fig. 8(b) are q_z scans taken for different values of q_x. For the larger values of q_x, the diffraction scan is sensitive to the higher-frequency corrugation of the interfacial roughness.[45] For all q_x values, the diffuse scans are peaked at the same q_z values, which indicates that the interfacial roughness is correlated for all frequencies explored. There is, however, a systematic broadening of the peak widths with increased q_x values. This implies that the lower-frequency components of the roughness are more strongly correlated than the higher-frequency components.[21,45]

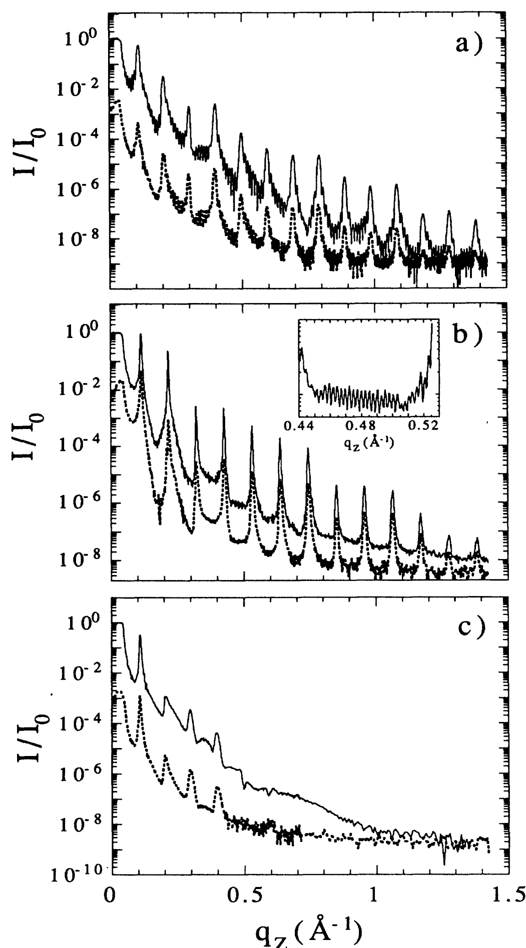

FIG. 7. Low-angle specular (solid line) and longitudinal diffuse (dashed line) scattering from (a) a 5-mTorr [Nb(35 Å)/Si(30 Å)]$_{10}$ multilayer, (b) a 3-mTorr [Nb(35 Å)/Si(30 Å)]$_{40}$ multilayer, and (c) a 15-mTorr [Nb(35 Å)/Si(30 Å)]$_{40}$ multilayer. The inset in (b) shows an expanded view of the specular intensity between the fourth and fifth Bragg reflections.

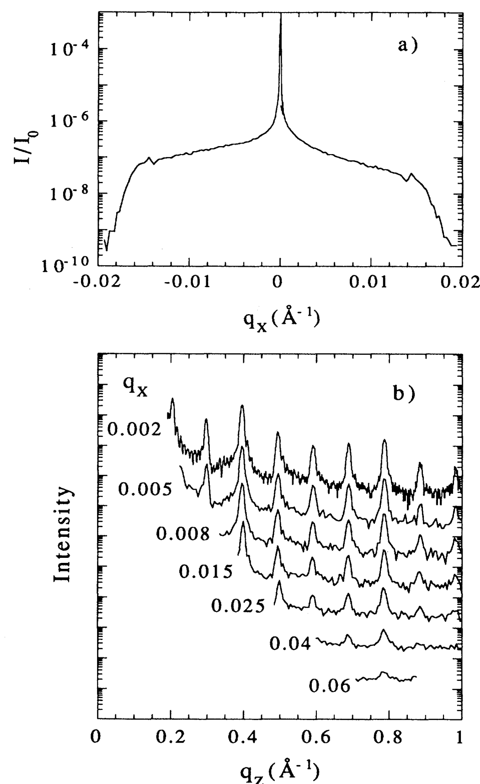

FIG. 8. (a) Transverse diffraction scan about the $q_z = 0.4$ Å^{-1} reflection of the 5-mTorr [Nb(35 Å)/Si(30 Å)]$_{10}$ multilayer in Fig. 7(a). (b) Longitudinal diffuse scans for the same sample for fixed q_x values, where $q_x = 0.0$ Å^{-1} corresponds to the specular intensity in Fig. 7(a). Each spectrum is offset by a decade from the prior scan.

V. LOW-ANGLE XRD MODELING

A. General description of the modeling

To quantify the structural parameters of the multilayers we fitted the specular reflectivities to a model based on the original optical formalism described by Parratt.[46] The reflectivity of a perfect interface is proportional to the difference in electron densities of the constituent layers, but is reduced by interdiffusion or roughness. For a Gaussian interface profile of width σ, the reflectivity is reduced by a factor $\exp(-2k_1k_2\sigma^2)$, where k_1 and k_2 are the wave vectors in the constituent layers.[43] To calculate the scattered intensity dynamically requires matching the boundary conditions at each interface and calculating the scattering from each interface recursively. In a kinematic

model, multiple reflections are ignored and the scattered intensity is given by summing the reflectivity of each interface with the proper absorption and phase information, including refraction.[21,39,41] The two formalisms are identical as long as the scattered intensity is $<10\%$ of the incoming intensity. The kinematic formalism breaks down near the critical angle and for intense Bragg reflections. The main advantages of the kinematic formalism are computational ease and the fact that cumulative layer-thickness errors can be incorporated easily within a closed-form expression as in wide-angle calculations.[24] For the following calculated intensities, we use a fully dynamical formalism below $q_z = 0.14$ Å^{-1} and a kinematic formalism above. All the calculated spectra are convoluted with an appropriate instrumental resolution function.

The XTEM images show no change in the interfacial profile vs thickness for the low-pressure multilayers. This is clearly not the case for the high-pressure multilayers. We have modeled the cumulative nature of their roughness in two ways: (i) By assuming that the interfacial width is constant and ensemble averaging the random, cumulative layer-thickness errors; and (ii) by assuming that the average layer thickness is constant and by increasing the interfacial width with an increased number of layers. Although these two approaches appear qualitatively different, the cumulative roughness parameter determined for these two models is the same. We will concentrate first on the results of model (i) because it is straightforward to incorporate this model within a kinematic formalism.[24,39] We assume that the thickness fluctuations about the average form a continuous Gaussian distribution of width σ_t. The fluctuations are assumed to be cumulative and the fluctuations of each layer are assumed to be statistically independent of the previous layers. The total scattering amplitude of the multilayer is given by integrating the scattering amplitude of particular layer-thickness configurations over all possible fluctuations. Since the measured intensity is the true specular, we average the scattering amplitude and not the scattered intensity.[37,39,47] [It would have been necessary to average the scattered intensity if the total intensity (specular plus diffuse) were to be calculated.] The specular intensity is then given by the square of the integrated amplitude. This result is equivalent to the expression from Ref. 39 for the specular reflectivity which includes cumulative roughness.

B. XRD analysis: Evidence for an interfacial compound and cumulative disorder

Results for the $N = 10$ multilayers are compared to experiment in Fig. 9. The peak widths are considerably broader than the instrumental resolution because of the limited number of layers. This simplifies the quantitative comparison of the measured and calculated intensities because such a comparison becomes less sensitive to resolution corrections. The spectra were least-squared fitted to model (i) by minimizing the difference between the logarithm of the measured and calculated intensities squared. This is accomplished by adjustment of the relative

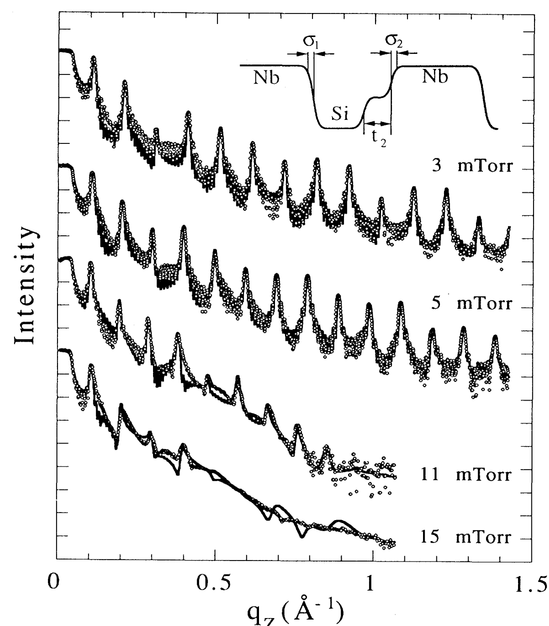

FIG. 9. Low-angle specular reflectivity scans (circles) and calculated reflectivities (line) for $[Nb(35\ Å)/Si(30\ Å)]_{10}$ multilayers sputtered at various Ar pressures. The inset shows schematically the interfacial profile used in the calculated reflectivities. Parameters used in the calculations are given in Table I.

thicknesses (t_{Nb} and t_{Si}), interfacial parameters, and substrate and surface roughnesses. When the 3- or 5-mTorr sample are fitted under the assumption that the Nb-on-Si and Si-on-Nb interfaces are equivalent, there are significant discrepancies between the calculated and measured spectra. If different widths are assumed for the Nb-on-Si and Si-on-Nb interfaces, then the fits are substantially improved, however there are still a number of discrepancies between the measured and fitted spectra. To further refine the fitting model, we used the results of TEM studies of the metal/Si superlattice which have shown that the interface compounds can form at the interface.[28,30,31] The inset in Fig. 9 schematically shows the interfacial profile assuming an interfacial compound reaction. The solid lines in Fig. 9 show fitting results which allow for the interfacial profile given by the inset. The spectrum is best fitted by a Si-on-Nb interface of width σ_1 and including an interfacial compound of thickness $t_2 \approx 4$ Å with an intermediate scattering power of 1.6 ± 0.3 as compared to 2.3 for bulk Nb and 0.7 for Si. This results in there being effectively two interfaces (with widths given by σ_2) at each Nb-on-Si interface in the calculation.

This model is able to reproduce both the multilayer peaks and the finite-size peaks over eight decades in intensity. Parameters of the model are given in Table I. The low values of σ_t for the low-pressure samples are in agreement with the analysis of the XTEM images in that they show little increase in roughness normal to the layers. The values for $\sigma_1 = 1.5$ Å and $t_2 = 4$ Å are in quantitative agreement with similar studies of Mo/Si multilayers which found the Si-on-Mo and Mo-on-Si interface

TABLE I. Fitting parameters for Nb/Si multilayers shown in Figs. 9–11, where t_{Nb} and t_{Si} are the average thicknesses of the Nb and Si layers, respectively, N is the number of bilayers, P_{Ar} is the Ar sputtering pressure, σ_1 is the half-width of the Si-on-Nb interface, σ_2 is the half-width of the interface on either side of the interfacial compound of thickness t_2 (see inset of Fig. 9), and σ_t is the cumulative thickness error of each layer.

t_{Nb} (Å)	t_{Si} (Å)	N	P_{Ar} (mTorr)	σ_1 (Å)	σ_2 (Å)	t_2 (Å)	σ_t (Å)
41	21	10	3	1.5	1.4	4.1	0.15
40	23	10	5	1.8	1.5	4.7	0.3
38	26	10	9	1.5	1.7	3.2	0.5
39	27	10	11	3.0	3.1		0.8
36	27	10	15	≈ 2	≈ 2		1.7
41	18	40	3	1.6	1.9	4.8	0.3
38	26	40	9	2.3	2	3.7	0.4
35	29	40	15	≈ 2.5	≈ 3		1.9
72	57	20	3	1.4	2.6	5.0	0.4
70	51	20	9	2.1	3.1	4.3	0.9

widths of 1.5 and 3.0 Å, respectively.[25] For the high-pressure multilayers (11 and 15 mTorr) the higher-order multilayer peaks are broadened or no longer resolved and the finite-size peaks quickly dampen out. As a result, the ability to resolve details of the interfacial profile is limited. The main difference in the fitting result is the increase in the cumulative thickness fluctuation per layer σ_t to 0.8 and 1.8 Å for increases in Ar pressure to 11 and 15 mTorr, respectively. For the high-pressure multilayers (11 and 15 mTorr) there was some additional intensity at $q \approx 0.5$ Å^{-1} which was not reproduced by the multilayer model. A similar feature was observed in the spectrum from a GaAs/AlAs superlattice.[41] By adding an additional layer of ≈ 10 Å to the top of the multilayer, we were able to reproduce this broad feature in the spectra. This additional layer may result from oxidation of the surface which is enhanced by the additional roughness and presence of grain boundaries.

The $N=40$ multilayers permit an evaluation of cumulative thickness errors relative to the $N=10$ multilayers. The $N=20$ multilayers permit the role of individual-layer thickness to be evaluated. Calculated and experimental results for the $N=40$ multilayers are shown in Fig. 10, and corresponding results for the $N=20$ multilayers appear in Fig. 11. The low-Ar-pressure samples are best fitted, again, by inclusion of an interfacial compound at the Nb-on-Si boundary. As the Ar pressure increases, the cumulative thickness-fluctuation parameter σ_t increases, is independent of the number of layers from 10 to 40 layers, but increases for the $N=20$ sample with increased layer thickness. Plotted in Fig. 12 is the cumulative thickness fluctuation σ_t for the $N=10$ and 40 samples as a function of Ar pressure. There is a break in the data at an Ar pressure of 9 mTorr, the same pressure at which thermalization of the sputtered atoms occurs.

Within the model described above, the layer-thickness fluctuation of each layer is cumulative but statistically independent from the previous layer, so that the interface fluctuations per interface scale by the square root of the number of interfaces. This leads to an effective $t^{0.5}$ scaling behavior of the cumulative roughness. For the 15-mTorr samples where $\sigma_t \approx 1.8$ Å, the interface fluctuations of the 10th and 40th bilayer are 8.5 and 17 Å, respectively. The XTEM images are consistent with these values. Figure 3(b), which depicts an expanded view of the 15-mTorr sample near the top of the multilayer, shows that the fluctuations of the interface positions are of the order of the Si thickness.

C. Modeling the interfacial width parameters

The second model we used to fit the diffraction spectra involved an increase in the interfacial width with an increased number of layers. In this way a more general scaling behavior of the roughness with layer thickness could be developed.[48] However, we were unable to obtain a unique solution for β when a t^{β} power-law scaling of the roughness was used in a general least-squares-fitting

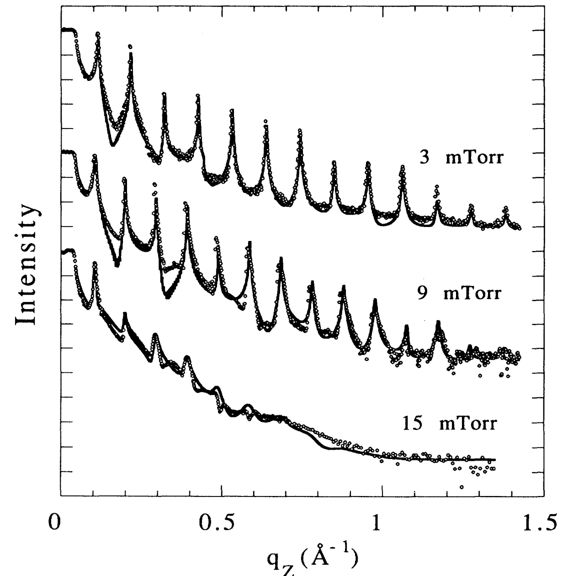

FIG. 10. Low-angle specular reflectivity scans (circles) and calculated reflectivities (line) for [Nb(35 Å)/Si(30 Å)]$_{40}$ multilayers sputtered at various Ar pressures. Parameters used in the calculations are given in Table I.

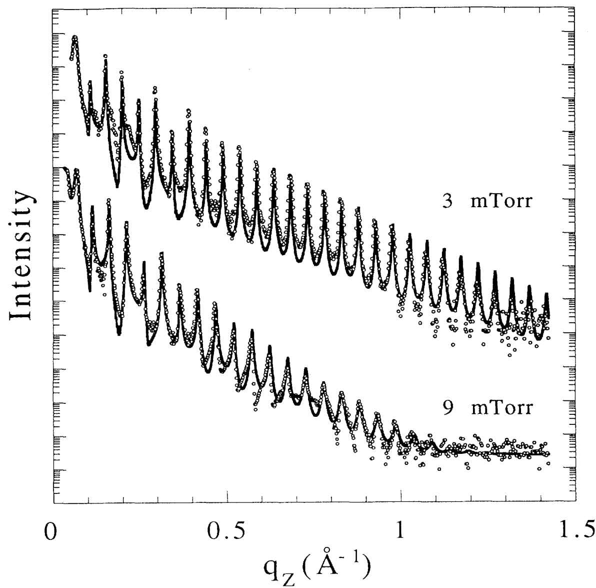

FIG. 11. Low-angle specular reflectivity scans (circles) and calculated reflectivities (line) for $[\mathrm{Nb}(70\ \text{Å})/\mathrm{Si}(60\ \text{Å})]_{20}$ multilayers sputtered at 3- and 9-mTorr Ar pressure. Parameters used in the calculations are given in Table I.

routine. Agreement with the measured spectrum was obtained by using $\beta=0.5$ and the interface parameter values from model (i) above. For example, Fig. 13 shows the results of the parameters of the $N=10$, 11-mTorr sample in Table I calculated using model (ii). The interfacial roughness of the jth interface in the multilayer σ_j is given by

$$\sigma_j^2=\sigma^2+j\sigma_t^2 , \tag{1}$$

where σ is the intrinsic roughness (σ_1 or σ_2 in Fig. 9) and σ_t is the cumulative roughness parameter. The calculation in Fig. 13 does not include the surface layers used in Fig. 9 so it does not reproduce the broad background intensity around $q\approx 0.5$ Å^{-1}. However, the result of the two models are equivalent in reproducing the measured peak widths and intensities and the parameters in Table I are insensitive to the particular model used.

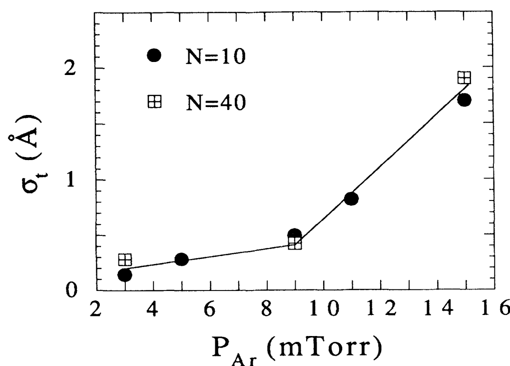

FIG. 12. Thickness errors σ_t vs Ar pressure for $[\mathrm{Nb}(35\ \text{Å})/\mathrm{Si}(30\ \text{Å})]_{10}$ (circles) and $[\mathrm{Nb}(35\ \text{Å})/\mathrm{Si}(30\ \text{Å})]_{40}$ (squares) multilayers.

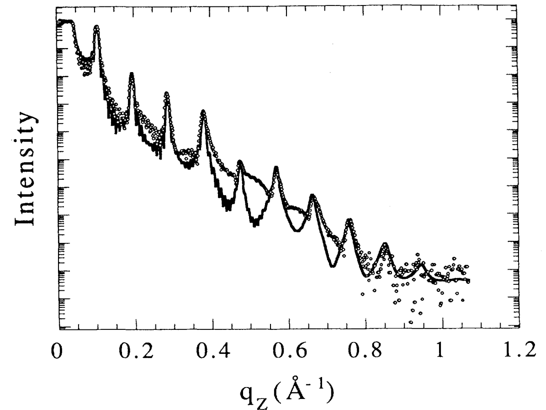

FIG. 13. Low-angle specular reflectivity scans (circles) and calculated reflectivities (line) for $[\mathrm{Nb}(35\ \text{Å})/\mathrm{Si}(30\ \text{Å})]_{10}$ multilayers sputtered at 11-mTorr Ar pressure. Parameters used in the calculations are given in Table I and discussed in the text.

VI. DISCUSSION

First we will discuss generalities of growth kinetics as it applies to our situation. We will then relate our observations to those in the literature, and consider prior modeling insights. The relationship to the film stress is briefly considered. Finally, we discuss thermodynamic considerations, with special interest in the role of the heat of mixing in understanding interfacial compound formation.

A. Growth kinetics

As can be seen from both XTEM and XRD, there is a qualitative change in the multilayer structure with increased Ar pressure. For the low-pressure sample, the layers are smooth over lateral distances $>1\ \mu$m with little increase in roughness with the number of layers. For higher Ar pressures, the roughness of the layers changes dramatically as the number of layers increases. Fluctuations in the layers, once initiated, grow into domed columns with well-defined grain boundaries. This transition occurs at roughly the expected pressure for thermalization of the sputtered atoms and dramatically demonstrates the role of kinetics on the morphology of the layers.

As the sputtering pressure is increased, scattering of the deposited atoms with the sputtering gas has two important consequences on the deposited atoms: (i) the oblique velocity component of the impinging atoms increases, and (ii) the average kinetic energy decreases.[22] Both of these effects will change the growth dynamics of thin films or multilayers and it is not clear which will have a larger effect. However, both changes tend to enhance the effects of self-shadowing and the formation of domed columns characteristic of zone-1 thin-film growth. On a rough surface, the valleys or low points on the surface will have a limited angle of acceptance for deposited atoms. As the oblique angle of the deposited atoms increases, the percentage of atoms within the acceptance angle decreases and preferred deposition occurs on the high points of the surface. If the surface mobility

is low, then the deposited atoms are unable to diffuse to the low points on the surface. As the growth progresses, the valleys grow deeper and form well-defined grain boundaries between broad growth fronts.

For lower Ar pressure, the sputtered atoms become more collimated with higher kinetic energy which reduces the effects of self-shadowing. The increased kinetic energy increases the surface mobility of the deposited atoms and leads to displacements of atoms on the growth surface. The growth surface can also become bombarded by reflected neutral gas atoms, electrons, and negatively charged ions. Reflected Ar neutrals are expected to have energies significantly higher than the adatoms.[25] Bombardment of the surface will preferentially affect the highest points of the surface and suppress columnar growth. It has been observed that interfaces can be smoothed[36,49] and columnar growth can be suppressed by independent ion bombardment of the film surface during growth.[50] For very low sputtering pressures, displacements of the surface atoms into the interior also can occur by forward sputtering. The expectation that the columnar structure will be suppressed is seen clearly in the XTEM comparison of Figs. 2 and 3. Increased surface mobility should also result in the growth of oriented Nb(110) grains.[25] Metal films typically grow, given sufficient surface mobility, normal to the densest atomic plane to minimize the surface energy. When the Ar pressure is high and surface mobility is low, it would be expected that small randomly oriented grains would nucleate resulting in a polycrystalline Nb layer. For higher surface mobility, the adatoms can arrange to minimize the surface energy and form large Nb(110) grains. The transition from oriented Nb(110) grains to polycrystalline Nb layers with increased Ar pressure is seen in the wide-angle data in Fig. 5.

The XTEM images shown in Figs. 2 and 3 are for the extreme pressure ranges of our study. The XRD results in Figs. 5–13 quantify the transition from low to high pressure. Both the low-angle and wide-angle XRD results vary systematically with Ar pressure. The low-pressure films have smooth layers with limited cumulative roughness (i.e., small σ_t) and highly oriented (110) grains. As the Ar pressure increases, there are only small increases in both σ_t and the wide-angle rocking-curve width up to 9 mTorr. This result is consistent with the XTEM images of the 9-mTorr sample, which is qualitatively more similar to that of the 3-mTorr than the 15-mTorr sample. Although the changes are small, the difference between the 3- and 9-mTorr samples is seen clearly in the low-angle XRD spectra. Above 9 mTorr, there is a much more dramatic change in both σ_t and the wide-angle rocking-curve width. In fact, the shapes of Figs. 12 and 5(b) look nearly identical, indicating that the surface morphology and crystalline microstructure are highly correlated. This is not surprising, since both the microstructure and morphology depend similarly on the surface mobility of the deposited adatoms.

B. Prior modeling overview

The scaling of this zone-1 type of growth has been studied theoretically based on a Huygens-principle growth mechanism[12] and Monte Carlo simulations.[13] It is found that as the growth progresses, the width of the domed columns increases and follows a power-law behavior, with the exponent depending sensitively on the initial surface topology. As the width of the columns increases, some grain boundaries merge to accommodate the lateral growth of the grains. Figure 2 of Ref. 12 shows the evolution of a random initial surface according to the Huygens-principle model, and Fig. 4 of Ref. 13 shows results of Monte Carlo simulations. Both cited references appear to be in qualitative agreement with the information contained in the XTEM images of the 15-mTorr sample. Unfortunately, the multilayer thicknesses studied herein (2500 Å) are not sufficiently thick to investigate the later stages of grain growth to determine an accurate scaling exponent.

For theoretical models in which there is a competition between shadowing and surface diffusion, it is found that the growth of a smooth surface will initially continue to be smooth up to a critical height which is dependent on the surface diffusion constant.[51] Above this height, the surface roughens and forms a columnar structure. A similar transition height was calculated in the Monte Carlo simulations of Ref. 13. This prediction also appears to be in qualitative agreement with the XTEM image of the 15-mTorr sample, where the first four bilayers appear smooth. Additionally, the formation of the columns does not seem to be related to defects in the substrate as has been observed in other studies.[17]

A transition is often observed in the intrinsic stress of the film sputtered at different Ar pressures which is thought to be related to the growth kinetics in a similar way as the interface morphology.[22] For low-pressure deposition, the intrinsic stress is compressive; it becomes tensile for higher pressure. The transition occurs at an Ar-pressure target-substrate distance product of ≈ 60 mTorr cm for both Cu and Mo films. This corresponds to an Ar pressure of ≈ 6.5 mTorr for our system, and is near the expected thermalization pressure. The compressive stress at low pressure is usually attributed to an atomic peening mechanism, and the tensile stress is thought to result from the relaxation of grain boundaries which are formed at high sputtering pressures. Other physical properties of thin films have been found to vary significantly with Ar pressure, including resistivity, reflectivity, and Ar incorporation.[22]

C. Thermodynamics of interfacial compound formation

Some care is needed in applying only kinetics arguments to sputtered multilayers. The growth of multilayer structures also depends strongly on the thermodynamic properties of the constituent materials. As was pointed out by Clemens and Sinclair,[3] multilayer growth should depend on the heat of mixing of the constituents. For systems with positive heats of mixing, sufficient mobility of the atoms can result in islanding and give poor layering. Conversely, systems with a large negative heat of mixing will result in layer nucleation and growth for high mobility. This argument is certainly consistent with our Nb/Si-multilayer results in which there is a large nega-

tive heat of mixing. There is clearly evidence of mixing at the Nb-on-Si interface, which is consistent with a number of other studies on metal/Si multilayers which show asymmetries in the interfacial profiles. Compound reaction may actually help to smooth the interface, by going from a rough interface towards a more uniform compound layer. Smoothing of substrate roughness has been observed in sputtered W/C multilayers.[20]

The asymmetry in the interfacial profile has been observed for a number of metal/Si and metal/metal[52] multilayer systems. This difference has been attributed to a number of factors including (i) the higher kinetic energy of the metal adatoms impinging on the Si surface,[31,52] (ii) the difference in latent heat of condensation,[29] or (iii) enhanced Si diffusion into the forming metal layer relative to diffusion into the already deposited metal layer.[28] Since we observe no significant difference in the local interface widths as determined by XTEM with increased Ar pressure, the kinetic energy of the deposited atoms does not seem to play a major role. Additionally, interfacial compound reactions have been observed in evaporated films where the kinetic energy of the deposited atoms is considerably lower than that of sputtered atoms.

There is considerable experiment work on the phase reaction at metal-amorphous Si interfaces.[2,53] However, the kinetic and thermodynamic constraints on phase selection during growth are not well understood. For some systems crystalline interfacial compounds are formed (e.g., Co/Si, Cr/Si) and for others the first compound is amorphous (e.g., Ti/Si, Ni/Si). For sputtered Fe/Si multilayers, the interfacial compound can be either crystalline or amorphous depending on the Si-layer thicknesses.[54,55] Additionally, for Fe/Si multilayers, the interfacial reaction occurs in two stages: (i) Si diffuses into the bcc-Fe layer up to the solubility limit (≈ 15 at. % Si in α-Fe), and (ii) it then forms a nonmagnetic Fe-Si phase at the interface. The initial diffusion of Si lowers the interfacial energy, which may, in turn, limit the amount of compound reaction. This mechanism was suggested to explain the interface reaction in Ni/*a*-Si multilayers.[53]

As seen in Table I, the Nb-layer thicknesses are larger than the thin film and design values, and the Si-layer thicknesses are less than the design thicknesses of ≈ 30 Å. Similar changes in the layer thicknesses from the designed values have been observed in Mo/Si (Ref. 36) and Ru/Si multilayers.[26] For multilayers in which the nominal layer thicknesses were doubled, the measured layer thicknesses were closer to their expected values. Reaction between the Nb and Si can explain qualitatively why (i) the Nb- and Si-layer thicknesses differ from the expected values, and (ii) the crystal coherence length of the Nb layers is significantly smaller than the layer thickness. The reduced coherence length implies that the compound formed is amorphous, similar to Mo/Si multilayers.[28] The first expected phase to form is $NbSi_2$.[56] Since this phase is Si rich, its formation will tend to decrease the Si-layer thickness and increase the Nb thickness relative to a perfect interface. Additional diffusion of Si into the Nb layer also will increase the Nb-layer thickness and decrease the Si thickness. This type of diffusion is not unreasonable given that significant diffusion of Si into Mo has been observed, even for MBE growth of Mo on single-crystal Si substrates at room temperature.[57] Annealing these multilayer structures results in a reduction in Λ with increased annealing temperatures due to the continued reaction of the metal and Si layers. To reduce these effects, MoSi/Si multilayers have been made to inhibit Si diffusion into the Mo layer in an attempt to retain the deposited layer thicknesses.[36] Although the formation of compounds at the interface is inferred from the XTEM and XRD results, additional diffusion of Si into the Nb layers is difficult to determine with these techniques. To resolve this effect would require an element-sensitive technique, such as Mössbauer spectroscopy as used to study Fe/Si multilayers,[54,55] or Auger spectroscopy as used to study the Mo-on-Si system.[57]

D. Relationship to other physical properties

Although the interface morphology of the low- and high-pressure samples changes, the interfacial width determined locally from the digitized XTEM images is not significantly different. The main difference results from fluctuations in the interfacial position over lateral distances ≈ 100 Å. This difference in lateral length scale has to be considered when addressing the effects of interfacial structure on the physical properties of the multilayers. For example, surface acoustic-phonon-velocity measurements for the low- and high-pressure Nb/Si multilayers show the same dependence on layer thickness.[58] But since acoustic phonons average over length scales of ≈ 5000 Å, such short-range fluctuation of the interface positions has little effect on the elastic response. Transport properties will be dependent on both the local interfacial structure and morphology. Some care is needed when using average interfacial widths for understanding physical properties. For example, the effects of interface roughness on the magnitude of the giant magnetoresistance in Fe/Cr superlattices is presently an open question. Different techniques have been used to change the interface "roughness" such as varying the Ar pressure,[18,59] superlattice thickness, or sputtering rate,[18] codepositing Fe and Cr at the interface or thermal annealing to increase the interdiffusion,[60] and changing the substrate temperature.[61] Clearly, the effects of changing the Ar pressure, which alters the interface morphology but does not significantly alter the interdiffusion,[62] are qualitatively different from codepositing Fe and Cr at the interfaces. In general, characterization should try to separate the contributions of roughness (including lateral length scales) and interdiffusion, and changes in the atomic structure of the interface.

VII. CONCLUSION

We have studied the interfacial structure of Nb/Si multilayers as a function of Ar sputtering pressure. We find that interfacial roughness and crystalline microstructure vary systematically with pressure with a clear transition in the growth dynamics at an Ar pressure of 9

mTorr. Multilayers sputtered at low Ar pressures (< 9 mTorr) form smooth flat layers with limited increase in the interfacial roughness with film thickness, and possess (110)-textured Nb grains. For multilayers sputtered at high pressures (> 9 mTorr), the initial layers are smooth, but, as the growth progresses, fluctuations in the layer thickness develop into domed columns with well-defined grain boundaries characteristic of zone 1 thin-film growth. The transition pressure, ≈9 mTorr, corresponds to the expected thermalization pressure of the sputtered atoms. For low-pressure multilayers, the XRD spectra are best fitted with a model that includes asymmetric widths of the interfaces. The Si-on-Nb interface is sharper than the Nb-on-Si interface. This conclusion is in agreement with XTEM results which also show that the interfacial widths are roughly independent of the Ar pressure but are asymmetric. The low-angle XRD modeling was used to quantity cumulative layer-thickness-fluctuation and interfacial-width parameters, as well as to identify the existence of an interfacial compound at the Nb-on-Si interface. The interfacial compound can be understood based on thermodynamic stability arguments that consider the heat of mixing as the relevant gauge. The present work shows the dramatic effects that kinetics and thermodynamics have on interfacial morphology, the need to characterize both the diffusion and roughness of the interface, and the complementary nature of XRD and XTEM on the characterization of multilayers.

ACKNOWLEDGMENTS

Work supported by the U.S. Department of Energy, BES–Materials Sciences, under Contract No. W-31-109-ENG-38 at Argonne National Laboratory. Brookhaven National Laboratory is supported by the Department of Materials Research by the U.S. Department of Energy under Contract No. DE-AC02-76CH00016. We would like to thank the Brookhaven physics x-ray group for the use of their beamline X-22C.

[1] *Physics, Fabrication, and Applications of Multilayered Structures,* edited by P. Dhez and C. Weisbuch (Plenum, New York, 1988).

[2] See various articles in *Kinetics of Ordering and Growth at Surfaces,* edited by Max G. Lagally (Plenum, New York, 1990).

[3] B. M. Clemens and R. Sinclair, MRS Bull. **15**, 19 (1990).

[4] F. Family, Physcia A **168**, 561 (1990).

[5] M. Kardar, G. Parisi, and Y. Zhang, Phys. Rev. Lett. **56**, 889 (1986).

[6] H. Yan, Phys. Rev. Lett. **68**, 3048 (1992).

[7] S. Das Sarma and P. Tamborenea, Phys. Rev. Lett. **66**, 325 (1991).

[8] H. You, R. P. Chiarello, H. K. Kim, and K. G. Vandervoort, Phys. Rev. Lett. **70**, 2900 (1993).

[9] Y.-L. He, H.-N. Yang, T.-M. Lu, and G.-C. Wang, Phys. Rev. Lett. **69**, 3770 (1992).

[10] J. Chevrier, V. Le Thanh, R. Buys, and J. Derrien, Europhys. Lett. **16**, 737 (1991).

[11] A. Duparré, J. Mod. Opt. **38**, 2413 (1991).

[12] C. Tang, S. Alexander, and R. Bruinsma, Phys. Rev. Lett. **64**, 772 (1990).

[13] A. Mazor, D. J. Srolovitz, P. S. Hagan, and B. G. Bukiet, Phys. Rev. Lett. **60**, 424 (1988).

[14] J. M. Thijssen, H. J. F. Knops, and A. J. Dammers, Phys. Rev. B **45**, 8650 (1992).

[15] R. A. Roy and R. Messier, in *Plasma Synthesis and Etching of Electronic Materials,* edited by R. P. H. Chang and B. Abeles, MRS Symposia Proceedings No. 38 (Materials Research Society, Pittsburgh, 1985), p. 363.

[16] G. L. M. K. S. Kahanda, X. Zou, R. Farrell, and P. Wong, Phys. Rev. Lett. **68**, 3741 (1992).

[17] D. J. Miller, K. E. Gray, R. T. Kampwirth, and J. M. Murduck, Europhys. Lett. **19**, 27 (1992).

[18] E. E. Fullerton, D. M. Kelly, J. Guimpel, I. K. Schuller, and Y. Bruynseraede, Phys. Rev. Lett. **68**, 859 (1992).

[19] D. E. Savage, N. Schimke, Y.-H. Phang, and M. G. Lagally, J. Appl. Phys. **71**, 3283 (1992).

[20] Ph. Houdy, P. Boher, C. Schiller, P. Luzeau, R. Barchewitz, N. Alehyane, and M. Quahabi, Proc. SPIE **984**, 95 (1988).

[21] D. G. Stearns, J. Appl. Phys. **71**, 4286 (1992).

[22] For a general discussion see H. Windischmann, CRC Crit. Rev. Solid State Mater. Sci. **17**, 547 (1992), and references therein.

[23] J. E. Mattson, M. E. Brubaker, C. H. Sowers, M. Conover, Z. Qui, and S. D. Bader, Phys. Rev. B **44**, 9378 (1991).

[24] E. E. Fullerton, I. K. Schuller, H. Vanderstraeten, and Y. Bruynseraede, Phys. Rev. B **45**, 9292 (1992).

[25] D. G. Stearns, R. S. Rosen, and S. P. Vernon, J. Vac. Sci. Technol. A **9**, 2662 (1991).

[26] D. L. Windt, R. Hull, and W. K. Waskiewicz, J. Appl. Phys. **71**, 2675 (1992).

[27] B. M. Clemens, J. Appl. Phys. **61**, 4525 (1987).

[28] J. M. Slaughter, P. A. Kearney, D. W. Schulze, C. M. Falco, C. R. Hills, E. B. Saloman, and R. N. Watts, Proc. SPIE **1343**, 73 (1990).

[29] K. Holloway, K. B. Do, and R. Sinclair, J. Appl. Phys. **65**, 474 (1989).

[30] D. G. Stearns, M. B. Stearns, Y. Cheng, J. H. Stith, and N. M. Cegilio, J. Appl. Phys. **67**, 2415 (1990).

[31] A. K. Petford-Long, M. B. Stearns, C.-H. Chang, S. R. Nutt, D. G. Stearns, N. M. Ceglio, and A. M. Hawryluk, J. Appl. Phys. **61**, 1422 (1987).

[32] D. L. Windt, R. Hull, W. K. Waskiewicz, and J. B. Kortright, Proc. SPIE **1343**, 292 (1990).

[33] See, for example, T. D. Nguyen, R. Gronsky, and J. B. Kortright, J. Electron Microsc. Tech. **19**, 473 (1991); W. C. Shih and W. M. Stobbs, Ultramicroscopy **35**, 197 (1991).

[34] Y. Ijdiyaou, M. Azizan, E. L. Ameziane, M. Brunel, and T. A. Nguyen Tan, Appl. Surf. Sci. **55**, 165 (1992).

[35] B. Heidemann, T. Tappe, B. Schmiedeskamp, and U. Heinzmann, Thin Solid Films **228**, 60 (1993).

[36] A. Kloidt, H. J. Stock, U. Kleineberg, T. Döhring, M. Pröpper, B. Schmiedeskamp, and U. Heinzmann, Thin Solid Films **228**, 154 (1993).

[37] W. Sevenhans, M. Gijs, Y. Bruynseraede, H. Homma, and I. K. Schuller, Phys. Rev. B **34**, 5955 (1986).

[38] S. K. Sinha, Physica B **173**, 25 (1991).

[39] A. P. Payne and B. M. Clemens, Phys. Rev. B **47**, 2289 (1993).

[40]D. E. Savage, J. Kleiner, N. Schimke, Y.-H. Phang, T. Jankowski, J. Jacobs, R. Kariotis, and M. G. Lagally, J. Appl. Phys. **69**, 1411 (1991).
[41]M. K. Sanyal, S. K. Sinha, A. Gibaud, S. K. Satija, C. F. Majkrzak, and H. Homma, in *Interface Dynamics and Growth,* edited by K. S. Liang, MRS Symposia Proceedings No. 237 (Materials Research Society, Pittsburgh, 1992), p. 393.
[42]Y. H. Phang, D. E. Savage, T. F. Kuech, M. G. Lagally, J. S. Park, and K. L. Wang, Appl. Phys. Lett. **60**, 2986 (1992).
[43]S. K. Sinha, E. B. Sirota, S. Garoff, and H. B. Stanley, Phys. Rev. B **38**, 2297 (1988).
[44]E. E. Fullerton, J. Pearson, C. H. Sowers, S. D. Bader, M. K. Sanyal, X. Z. Wu, and S. K. Sinha (unpublished).
[45]Y. H. Phang, R. Kariotis, D. E. Savage, and M. G. Lagally, J. Appl. Phys. **72**, 4627 (1992).
[46]L. G. Parratt, Phys. Rev. **95**, 359 (1954).
[47]P. F. Miceli, C. J. Palmstøm, and K. W. Moyers, App Phys. Lett. **61**, 2060 (1992).
[48]D. G. Stearns, Appl. Phys. Lett. **62**, 1745 (1993).
[49]E. Spiller, Appl. Phys. Lett. **54**, 2293 (1989); Opt. Eng. **29**, 609 (1990).
[50]R. D. Bland, G. J. Kominiak, and D. M. Mattox, J. Vac. Sci. Technol. **11**, 671 (1974).
[51]R. P. U. Karunasiri, R. Bruinsma, and J. Rudnick, Phys. Rev. Lett. **62**, 788 (1989).
[52]Y. Huai, R. W. Cochrane, and M. Sutton, Phys. Rev. B **48**, 2568 (1993).
[53]C. V. Thompson, L. A. Clevenger, R. DeAvillez, E. Ma, and H. Miura, in *Thin Film Structures and Phase Stability,* edited by B. M. Clemens and W. L. Johnson, MRS Symposia Proceedings No. 187 (Materials Research Society, Pittsburgh, 1990), p. 61.
[54]E. E. Fullerton, J. E. Mattson, S. R. Lee, C. H. Sowers, Y. Y. Huang, G. Felcher, S. D. Bader, and F. T. Parker, J. Magn. Magn. Mater. **117**, L301 (1992).
[55]E. E. Fullerton, J. E. Mattson, S. R. Lee, C. H. Sowers, Y. Y. Huang, G. Felcher, S. D. Bader, and F. T. Parker, J. Appl. Phys. **73**, 6335 (1993).
[56]R. Pretorius, Vacuum **41**, 1038 (1990).
[57]J. M. Slaughter, A. Shapiro, P. A. Kearney, and C. M. Falco, Phys. Rev. B **44**, 3854 (1991).
[58]E. E. Fullerton, M. Grimsditch, and I. K. Schuller (unpublished).
[59]K. Takanashi, Y. Obi, Y. Mitani, and H. Fujimori, J. Phys. Soc. Jpn. **61**, 1169 (1992).
[60]F. Petroff, A. Barthélémy, A. Hamzié, A. Fert, P. Etienne, S. Lequien, and G. Greuzet, J. Magn. Magn. Mater. **93**, 95 (1991).
[61]S. S. P. Parkin and B. R. York, Appl. Phys. Lett. **62**, 1842 (1993).
[62]D. M. Kelly, E. E. Fullerton, F. T. Parker, J. Guimpel, Y. Bruynseraede, and I. K. Schuller, Int. J. Mod. Phys. B **7**, 419 (1992).

(a)

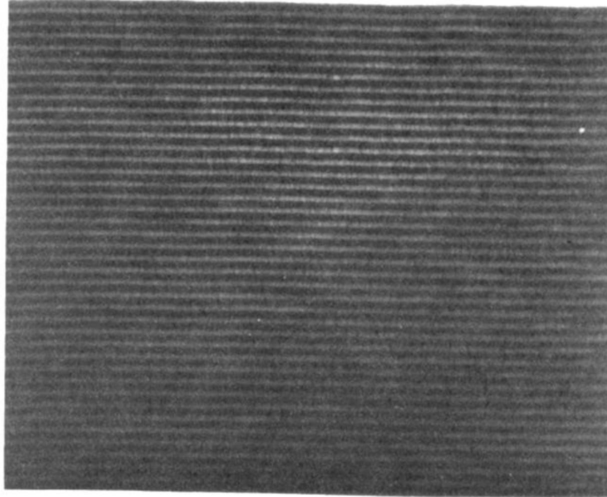

(b)

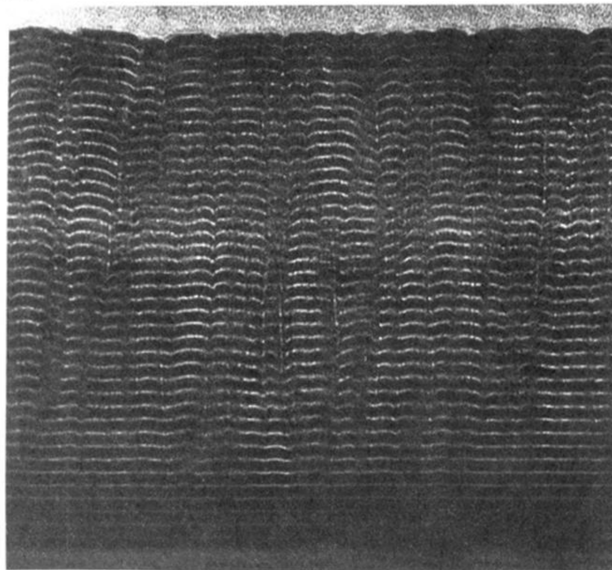

FIG. 2. XTEM images of [Nb(35 Å)/Si(30 Å)]$_{40}$ multilayers sputtered in (a) 3 mTorr and (b) 15 mTorr of Ar.

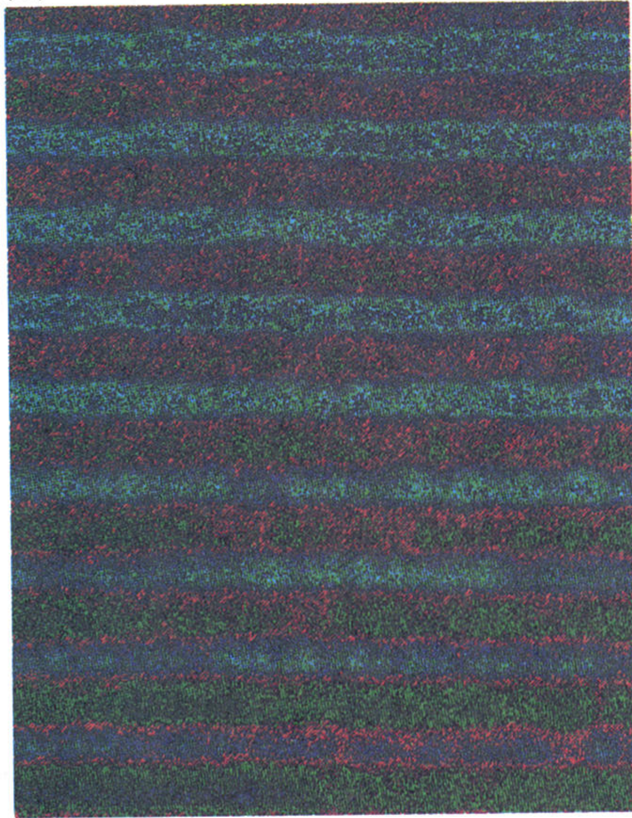

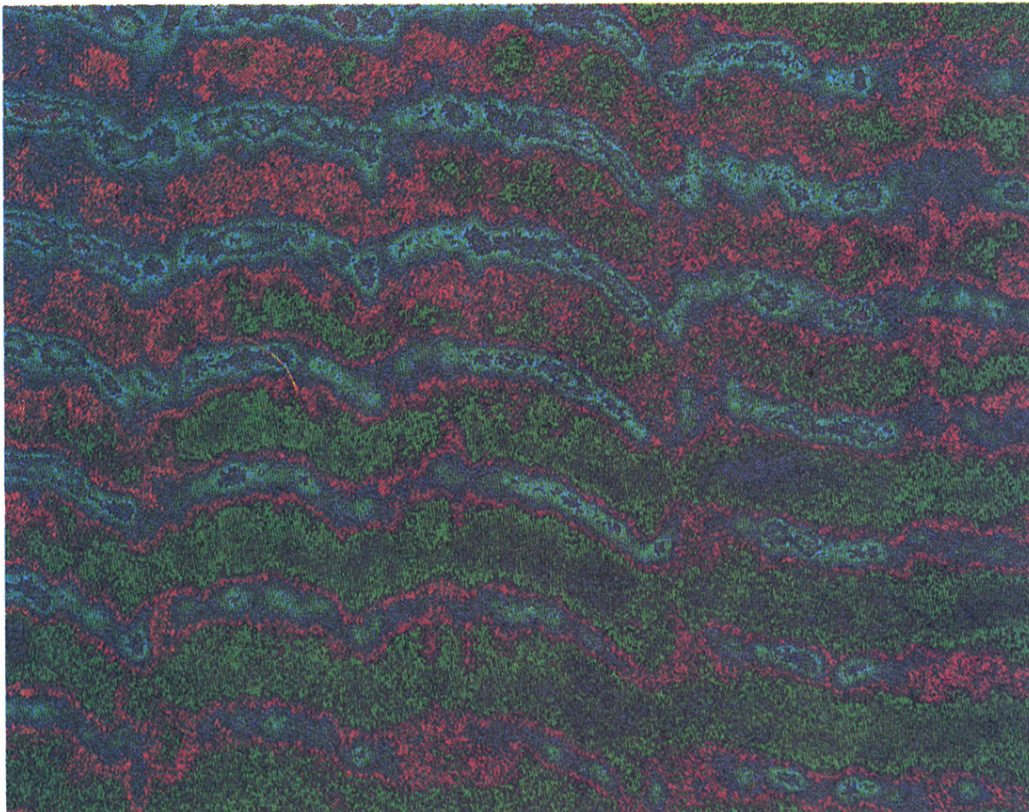

FIG. 3. Digitized and pseudocolor enhanced XTEM images from Fig. 1 corresponding to multilayers sputtered in (a) 3 mTorr and (b) 15 mTorr of Ar.